Available online at www.sciencedirect.com
SCIENCE DIRECT®
ELSEVIER
Nuclear Instruments and Methods in Physics Research A 547 (2005) 24–41
NUCLEAR INSTRUMENTS & METHODS IN PHYSICS RESEARCH Section A
www.elsevier.com/locate/nima

X-ray photoelectron spectroscopy and diffraction in the hard X-ray regime: Fundamental considerations and future possibilities

Charles S. Fadley[a,b,*]

[a]Department of Physics, University of California Davis, Davis, CA 95616 USA
[b]Materials Sciences Division, Lawrence Berkeley National Laboratory, Berkeley, CA 94720, USA

Abstract

The prospects for extending X-ray photoelectron spectroscopy (XPS) and X-ray photoelectron diffraction (XPD) measurements into the hard X-ray regime of 5–15 keV excitation energies are discussed from a fundamental point of view, in some cases using prior results obtained in the 1–2 keV range as starting points of discussion, together with theoretical estimates of behavior at higher energies. Subjects treated are: the instrumentation improvements needed to optimize peak intensities; the tuning of experimental conditions to achieve bulk or surface sensitivity; the use of grazing incidence to suppress spectral backgrounds; the use of standing waves created by Bragg reflection from crystal planes or synthetic multilayers to achieve position-sensitive densities of states, compositions, and magnetizations; photoelectron diffraction and Kikuchi-band effects as element-specific local structure probes; and valence-level measurements, including the role of non-dipole effects and mechanisms leading to complete Brillouin zone averaging and density-of-states like spectra. Several distinct advantages are found for such high-energy extensions of the XPS and XPD techniques.

PACS: 68.49.Uv; 79.60.−i; 61.14.Qp; 73.20.−r; 71.20.−b

Keywords: Photoelectron spectroscopy; Photoelectron diffraction; Electronic structure; Hard X-rays; Synchrotron radiation

---

1. Introduction

X-ray photoelectron spectroscopy (XPS or ESCA) is by now a very widely used technique for characterizing the surface and bulk properties of a broad variety of materials. Although the first measurements of this kind by Siegbahn et al. in the mid-1950s were actually carried out with photon

---

[*]Department of Physics, University of California Davis; Materials Sciences Division, Lawrence Berkeley National Laboratory, 1 Shields Ave., Davis, CA 95616 USA. Tel.: +1 530 7521500; +1 530 7524717.
E-mail address: fadley@physics.ucdavis.edu.

0168-9002/$ - see front matter © 2005 Published by Elsevier B.V.
doi:10.1016/j.nima.2005.05.009

energies in the 5–8 keV range [1], the desire for higher-energy resolution led immediately to a focus on excitation sources such as Mg Kα (1253.6 eV) and Al Kα (1486.7 eV), sometimes together with a crystal monochromator [1]. The development of synchrotron radiation (SR) sources over the past few decades has extended the energy range downward, erasing the distinction between ultraviolet photoelectron spectroscopy (UPS) and XPS and has by now provided energy resolutions below 0.1 eV, with corresponding enhancements in the ability to study chemical shifts, multiplets splittings, and other fine structure in both core and valence spectra. Along the way, however, it was suggested by Pianetta and Lindau in 1974 that high-resolution XPS could be profitably carried out in the 5–15 keV range with SR [2], an idea that has only recently been revived by several groups and demonstrated experimentally [3], as discussed in other articles in this issue.

In this article, I will discuss some fundamental considerations of carrying out XPS and the closely related technique of X-ray Photoelectron (XPD) in the hard X-ray regime, including instrumental considerations, what additional types of information might be gained from such measurements in the future, and certain limitations and special characteristics. In several instances, I will use data obtained at current typical excitation energies of about 1.5 keV to illustrate effects that should be useful when obtained with excitation in the 5–15 keV regime, together with theoretical estimates of how these effects will manifest themselves at these higher energies.

2. Photoelectron intensities

A primary reason for which hard X-ray photoelectron spectroscopy (HXPS) has not been more widely practiced to date is the general conclusion that intensities would be too low. Thus, a brief overview on this point is worthwhile. Although the argument will be presented for core-level intensities, the basic ideas also apply to valence levels. Fig. 1(a) illustrates the basic physical process involved, including the effects of both inelastic scattering and elastic scattering.

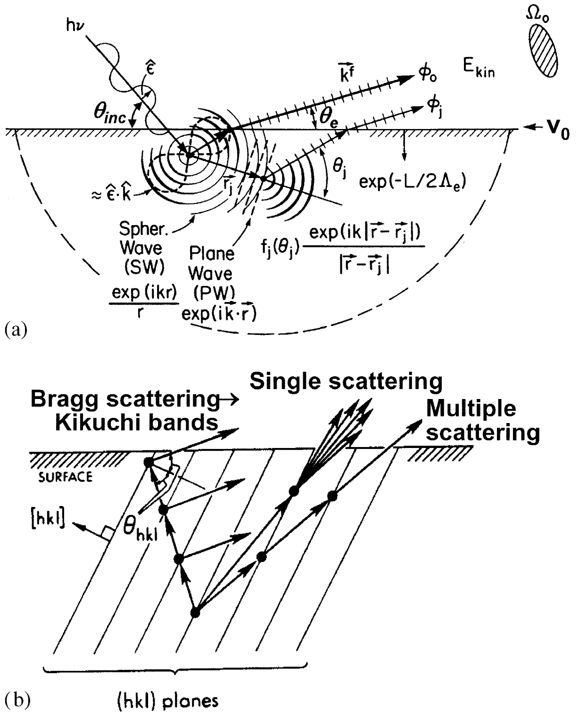

Fig. 1. (a) The basic physical process in X-ray photoelectron excitation by radiation with polarization $\hat{\varepsilon}$, including elastic scattering in either the plane-wave, or more accurate spherical wave, approximations; inelastic scattering through an attenuation length Λ_e; escape across the surface barrier (inner potential) V_0, and entry into the final acceptance solid angle of the spectrometer Ω_0. For s subshells and in the dipole approximation, the initial outgoing wave has an angular form proportional to $\hat{\varepsilon}\cdot\hat{k}$, with $\hat{k}$ a unit vector in the direction of propagation. (b) Illustration of additional Bragg-like scattering processes which arise for higher energies of excitation, leading to Kikuchi-band behavior. Multiple scattering must also be considered in accurately modeling all elastic scattering effects.

The intensity of a photoelectron peak from a given spin–orbit-split level $n\ell j$ associated with an atom Q in a homogeneous polycrystalline sample will in general be given by [4]

$$\begin{aligned} I(Qn\ell j) = {} & (\text{incident X} - \text{ray flux}) \\ & \times (\text{area of illuminated sample seen by analyzer}) \\ & (Qn\ell j \text{ differential photoelectric cross section}) \\ & \times (\text{solid angle accepted by analyzer}) \\ & \times (\text{density of atoms } Q) \\ & \times (\text{mean photoelectron escape depth}) \\ & \times (\text{overall detection efficiency}) \qquad (1) \end{aligned}$$

or in obvious notation,

$$I(Qnlj) = I_0(h\nu) \times A_0 \times (\mathrm{d}\sigma_{Qnlj}(h\nu)/\mathrm{d}\Omega) \times \Omega_0 \times \rho_Q \times \Lambda_{\mathrm{MED}}(E_{\mathrm{kin}}) \times D_0. \tag{2}$$

Here, we have emphasized the functional dependencies on photon energy or electron kinetic energy, as well as the optical properties of the electron energy analyzer, since the selective tuning of the latter is crucial to the future success of HXPS. The mean photoelectron escape depth $\Lambda_{\mathrm{MED}}(E_{\mathrm{kin}})$ in general must allow for both inelastic and elastic electron scattering, as updated recently by Jablonski and Powell [5], a point to which we return below. More approximately, $\Lambda_{\mathrm{MED}}(E_{\mathrm{kin}})$ can be replaced simply by the inelastic attenuation length $\Lambda_{\mathrm{e}}(E_{\mathrm{kin}})$.

Considering the factors here in order, we first note that third-generation SR undulators, combined with suitable hard X-ray monochromators, can provide highly intense ($\sim 10^{11}$–10^{12} photons/s) and monochromatic ($\Delta(h\nu) \leqslant 0.1\,\mathrm{eV}$) beams for HXPS. These can in turn be focused into a very small spot size of the order of tens of microns that can be well matched to the acceptance areas A_0 of current high-throughput and high-resolution analyzers. The key point here is that light which falls outside of the analyzer view is wasted. Of course, photoelectric cross-sections fall continuously as the energy is tuned above a given binding energy threshold, with approximate variations in a high-energy asymptotic, yet non-relativistic, approximation theoretically expected to be: $\sigma_{Qnlj}(h\nu) \propto (E_{\mathrm{kin}})^{-7/2}$ for s subshells and $\propto (E_{\mathrm{kin}})^{-9/2}$ for p, d, and f subshells [6(a)], and numerical tabulations of more accurate relativistic calculations of *total* subshell cross-sections $\sigma_{Qn\ell j}(h\nu)/\mathrm{d}\Omega$ for the entire period table and for photon energies from 1–100 keV have been published by Scofield [6(b)]. For several energies from 100–5000 eV and for heavier elements with $Z = 50-100$, Nefedov et al. have also calculated both relativistic cross-sections and the angular distribution_parameters that are essential for deriving the *differential* photoelectric cross-section $\mathrm{d}\sigma_{Qn\ell j}(h\nu)/\mathrm{d}\Omega$ [7].

The solid angle Ω_0 accepted by the analyzer is a property of the particular electron optical system, which usually includes some kind of retarding lens that magnifies the image A_0 by some factor M to an area at the entrance to the analyzer of $A' = MA_0$. A typical analyzer system is shown in Fig. 2, with the actual energy analysis section here being illustrated for the much-used hemispherical electrostatic configuration. The key tradeoffs in the retarding lens and the final energy analysis stage are governed by the Liouville Theorem, which dictates that source brightness before retardation B_0 and that after retardation B' must be related by

$$\frac{B'}{B_0} = \frac{E_{\mathrm{pass}}}{E_{\mathrm{kin}}} \tag{3}$$

where E_{kin} is the kinetic energy on leaving the sample and E_{pass} is the final energy of analysis.

Combining this with the conservation of electron flux on traversing the complete electron optical system finally yields via the Lagrange–Helmholtz relation to the form most convenient for this analysis:

$$A'\Omega'/A_0\Omega_0 = M\Omega'/\Omega_0 = E_{\mathrm{kin}}/E_{\mathrm{pass}} \equiv R, \tag{4}$$

where Ω' is the solid angle of acceptance after retardation and at the entry to the final energy analysis element, and R is the retardation ratio, which will generally be $\gg 1$ for HXPS measurements. This

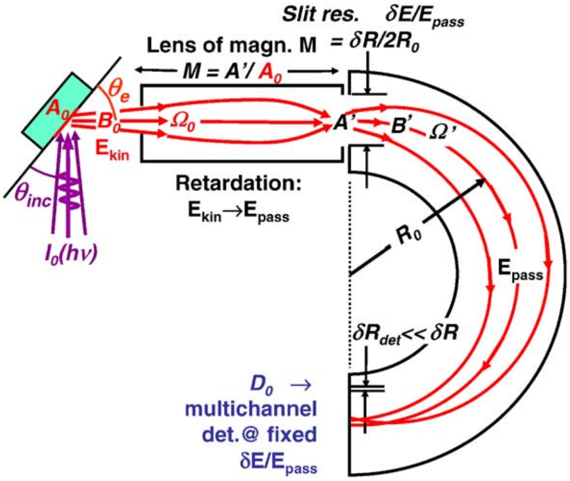

Fig. 2. The fundamental parameters controlling the final photoelectron intensity, here illustrated for the case of a hemispherical electrostatic analyzer with a retarding, imaging lens between it and the sample. Relevant symbols are defined in the text.

relationship of course only applies to those electron trajectories that pass through the entire electron optical system, allowing for the effects of any slits or collimators that may limit trajectories. A final important consideration is that the energy resolution of the final analysis stage $\delta E/E_{\mathrm{pass}}$ can be connected to Eq. (4) by

$$A'\Omega' \approx CR_0^2\,(\delta E/E_{\mathrm{pass}})^{1.5-2.0} \tag{5}$$

where we have assumed a hemispherical electrostatic analyzer as the final element, C is a constant characteristic of the type of analyzer, and R_0 is the radius of the central trajectory in the analyzer section. From Eqs. (4) and (5), we can see that, if A_0 is sufficiently small (as permitted by the highly focused SR beam), and R and M are sufficiently large, Ω_0 can be very large, while at the same time, via Eq. (5), A' and Ω' together can be maintained sufficiently small to obtain the desired final absolute energy resolution. Roughly speaking, retardation permits larger $A'\Omega'$ for a given desired energy resolution $\delta E/E_{\mathrm{kin}}$, and high magnification permits reducing Ω', again consistent with this resolution. Thus, the highly focused spot in a SR beamline, and carefully designed retarding electron optics with magnifications of 25 or higher, are crucial for the practical realization of HXPS, as discussed elsewhere [3].

Finally, being able to detect multiple energies in the final focal plane of the analyzer (cf. Fig. 2) is also crucial, as this effectively increases the factor D_0, with several approaches available for this: multiple channeltrons, microchannel plates (MCPs) coupled with resistive anodes or CCD detectors, and a newer approach based on MCPs with custom-designed integrated circuits [8]. Ideally, the width of each detector channel δR_{det} should be much smaller than the other contributions to resolution, as for example, that due to the entrance slit size δR in Fig. 2. Other articles in this issue will discuss more concrete examples of experimental systems based on these principles, but it is easy to estimate that intense core levels (e.g. Au 4f) will generate 10^4–10^5 electrons/s over the full spectrum, and even weaker valence bands have been successfully studied by now [3].

Thus, although cross-section dependence on photon energy as one goes into the hard X-ray regime is a serious handicap to HXPS, the availability of brighter SR sources, together with electron analyzer systems designed to take advantage of the small spot sizes involved and energy retardation before energy analysis, can compensate this so as to yield adequate data acquisition rates, as demonstrated in recent work.

3. Surface vs. bulk sensitivity

Certainly a primary attraction of HXPS is in increasing the ability to more accurately measure true bulk properties, and this is connected to the well-known energy variation of the electron inelastic mean free path $\Lambda_{\mathrm{e}}(E_{\mathrm{kin}})$, which at higher energies is expected to vary as $(E_{\mathrm{kin}})^{0.50-0.75}$ [5(b),9]. Simple geometric considerations then show that, if the electron exit angle with respect to the surface is θ_{e} (cf Fig. 1(a)), then the mean sensing depth of the measurement will go as $\Lambda_{\mathrm{e}}\sin\theta_{\mathrm{e}}$, thus providing a simple way of estimating, and varying, the degree of surface sensitivity. Thus, HXPS at roughly 10 keV should certainly be more bulk sensitive than measurements at 1 keV, with measurement depths 3–5 times larger. Again, for the example of metallic Au, $\Lambda_{\mathrm{e}}(E_{\mathrm{kin}})$ can be estimated to be about 70 Å at $E_{\mathrm{kin}} = 10\,\mathrm{keV}$ [9].

An accurate estimate of true measurement depths also needs to include the effects of elastic scattering, especially at lower kinetic energies [5]. This is because elastic scattering can cause electrons initially emitted at angles nearer to the surface normal to be scattered into angles further from the normal, and it is why the more accurate $\Lambda_{\mathrm{MED}}(E_{\mathrm{kin}})$ is included in Eqs. (1) and (2). Such effects have been discussed in detail previously [5], and they reduce the degree of surface sensitivity enhancement possible by going to lower electron exit angles relative to the surface. Such effects also complicate the interpretation of such data. However, an additional advantage of HXPS is that elastic scattering will be strongly peaked in the forward direction for 5–15 keV electrons, as will be discussed in more detail below, thus making the linear trajectory model that is involved in arriving at the $\Lambda_{\mathrm{e}}\sin\theta_{\mathrm{e}}$. estimate above a more accurate approximation [10].

A final effect to be considered in analyzing measurements with variable electron emission angles is the inner potential V_0 at the sample surface (cf. Fig. 1(a)). This has a value in the range 5–25 eV, and can significantly refract photoelectrons as they leave the surface [11], with this effect being worse for the grazing emission angles that are of greatest interest for enhancing surface sensitivity. However, going to hard X-ray excitation energies will much reduce this effect, making the interpretation of variable-angle HXPS data more straightforward in yet a second respect.

HXPS thus should not only be more bulk sensitive, but it should also permit more quantitative analyses of variable electron emission angle measurements so as to more quantitatively sort out bulk and surface effects. As a final word of caution, however, the expected mean emission depths in HXPS are still only ca. 50–100 Å, and small enough that consideration still must be given to surface contamination or surface reaction effects, especially for more reactive samples.

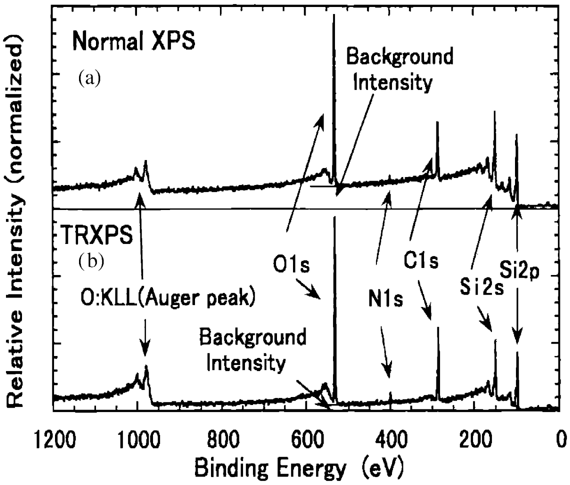

Fig. 3. Experimental data illustrating the reduction in elastic background that has been achieved in an XPS measurement on a Si surface with 1.5 keV excitation energy. (a) Normal XPS with a high X-ray incidence angle of 10°. (b) Total reflection XPS with a grazing incidence angle of 1° that is very close to the critical angle [14].

4. X-ray optical effects and total reflection

The effects of the onset of total X-ray reflection on photoelectron intensities were first discussed by Henke [12], and they eventually have led to the intentional use of total reflection geometries as a convenient tool for reducing the inelastic scattering background in XPS spectra [13]. As a recent example of the use of what has been termed total reflection XPS (TRXPS) or grazing-incidence XPS (GIXPS), I show in Fig. 3 broad-scan spectra obtained with Al Kα excitation from an HF-etched Si wafer with a high angle of incidence (10°, labeled Normal XPS) and with a low angle of incidence below the critical angle (1.1°, labeled TRXPS) [14]. The suppression of the inelastic background in the TRXPS spectrum is significant. Although all prior work of this type has been done in the typical XPS energy regime of about 1 keV, making use of total reflection to reduce what will probably be more significant inelastic backgrounds in spectra at 5–15 keV excitation energies appears to be very desirable, provided that the sample surface is flat enough to achieve the uniformly low average angles required. As some indication of how this might be achieved, Fig. 4 shows calculations for 10 keV photons incident on Au [15], and it is clear that the mean depth of excitation can be reduced to values that are comparable with the expected mean electron emission depth by going to incidence angles of 1° or less. Furthermore, as long as the mean depth of X-ray excitation is much greater that the mean emission depth of the photoelectrons, the full degree of bulk sensitivity can be achieved, but still with what should be spectra with much lower inelastic background intensity. This latter condition implies working somewhat above the critical angle. For the example in Fig. 4, an incidence angle of 1° that is about 2.5 times the critical angle would still yield an X-ray attenuation length about 10x larger than the estimated mean emission depth of the photoelectrons.

5. Standing wave studies of valence electronic structure and buried interfaces

Closely related to the X-ray optical effect discussed above is using Bragg reflectivity from a

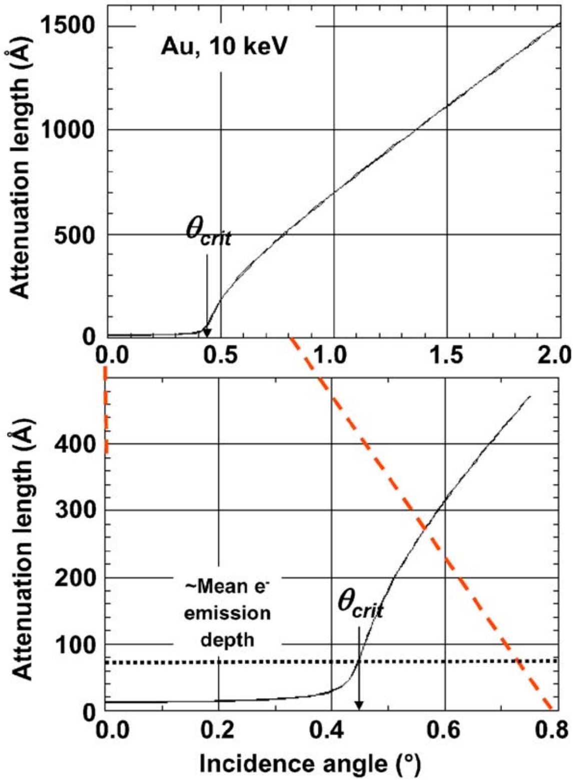

Fig. 4. Calculated X-ray attenuation lengths for 10 keV X-rays normal to a Au surface (via Ref. [15]), with the critical angle indicated, together with an estimate of the mean emission depth for 10 keV photoelectrons from this surface (dotted line, extrapolated from results of Ref. [9]). Dashed lines indicate the region in (a) that is expanded in (b).

set of crystal planes so as to set up a strong standing-wave modulation of the exciting electric field strength, and then rocking the crystal so as to move the standing wave with respect to the atomic positions. This has permitted Woicik and co-workers to study the site-specific valence-band structure of metal oxides, with obvious implications for future applications to other materials, especially if the photon energy is taken to higher values in the 5–15 keV regime [16]. This pioneering work is discussed in a separate article in this volume [17].

Beyond such crystal-plane Bragg reflections, it should also be possible to use reflections from synthetic multilayer structures to selectively tune the sensing depth in HXPS so as to study buried interfaces. To illustrate this, Fig. 5 shows a particular sample configuration which has recently been used in conjunction with soft X-ray excitation at about 1 keV to successfully study a buried interface between Fe and Cr that is of relevance to the giant magnetoresistance effect [18,19]. Here, the sample is grown on top of a synthetic multilayer mirror composed of 40 bilayers of B_4C and W, with a periodicity of 40 Å that will also be the period of the soft X-ray standing wave above the surface of the multilayer. The sample consists of a wedge of Cr and an overlayer of Fe of constant thickness. Since the focused X-ray spot is much smaller than the sample and the wedge slope is very small, it is possible to effectively scan the standing wave through the interface by scanning the sample in position along the direction of the slope of the wedge. By combining such sample scanning measurements with rocking curve measurements of Fe and Cr core photoelectron intensities, as well as with magnetic circular dichroism measurements for both Fe and Cr and comparing the data with X-ray optical calculations [19], it has been possible to determine the concentration profiles and magnetization profiles for both species through the buried interface, with final results as shown in Fig. 6 [18].

Standing-wave measurements of both types (crystal planes and multilayer structures) should be of considerable interest for HXPS studies. As one illustration of the strength of such standing wave effects in multilayer work, Figs. 7(a)–(b) show the reflectivity from a synthetic multilayer exactly like that used in the soft X-ray studies of Figs. 5 and 6, but at two incident energies of 1.0 and 10.0 keV, respectively. The reflectivity for soft X-rays is 0.28, while that for hard X-rays is a very high 0.80, which should yield much stronger modulations with depth than in the soft X-ray measurements. More quantitatively, if the X-ray reflectivity is denoted by $R_{h\nu}$, an approximate estimate of the total fractional modulation of the square of the standing-wave electric field intensity will be $4\sqrt{R_{h\nu}}$, as normalized to an incident wave field of unit strength. The bottom panels of Fig. 7 show the actual standing-wave modulation for these two energies as calculated with a program

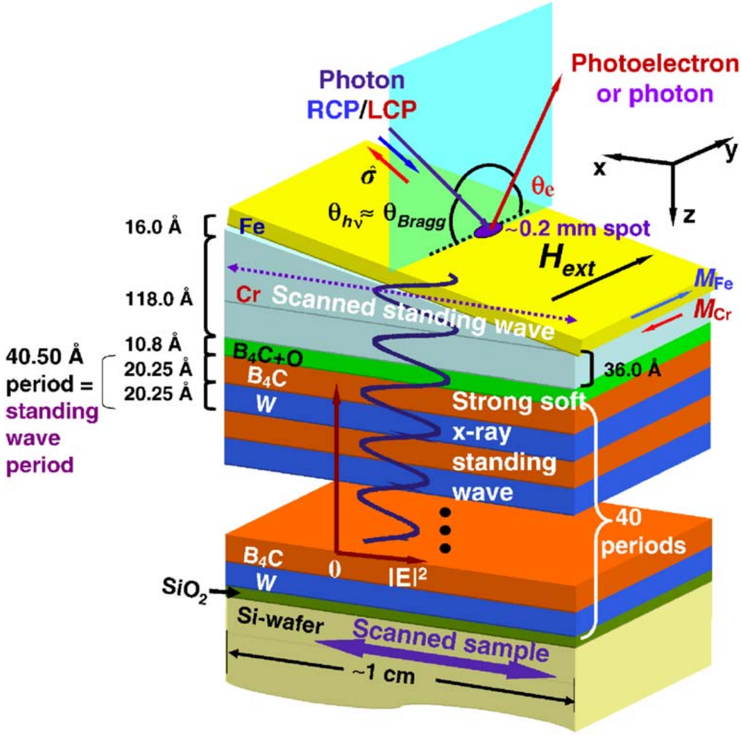

Fig. 5. Basic geometry for an experimental method that has recently been developed in the soft X-ray regime for probing buried interfaces [18]. Reflection from a multilayer mirror creates a strong standing wave above the mirror. One layer in a multilayer sample is grown in a wedge profile, permitting the scanning of the standing wave through various interfaces via the movement of the sample relative to the focused synchrotron radiation beam [18].

written by Yang [19] which includes the depth-dependent calculation of photoelectron intensities. For 1.0 keV, the overall modulation is 1.9 (compared with 2.1 from the simple $4\sqrt{R_{h\nu}}$ estimate) and for 10.0 keV it is 3.6 (compared with 3.6 from the simple estimate). For 10.0 keV, the standing wave minima are also very near zero, which should provide maximum contrast in deriving depth-dependent effects. Such studies with hard X-rays are thus most promising for the future.

6. Photoelectron diffraction

X-ray photoelectron diffraction (XPD) is by now a standard surface structure technique [20], so one can now ask what advantages and disadvantages would be associated with carrying it out at excitation energies of 5–15 keV. Fig. 1(a) illustrates the basic physics involved. An X-ray of polarization $\hat{\varepsilon}$ excites a photoelectron wave which propagates as a distorted spherical wave out to some scattering atom j located at position $\vec{r}_j$. A scattered-wave component proportional to the scattering factor $f_j(\theta_j)$ (with θ_j the scattering angle) then interferes with the unscattered component to produce the diffraction pattern. This interaction is summed over all the atoms in a suitable cluster neighboring a given type of emitter. Inelastic scattering acts to attenuate all wave components. It is also crucial to include multiple scattering of the photoelectron, with various programs now available for calculating such patterns at up to about ~2 keV kinetic energy [21].

Of course, one immediate benefit of going to much higher energy is that the probing depth would be increased, in principle allowing for the

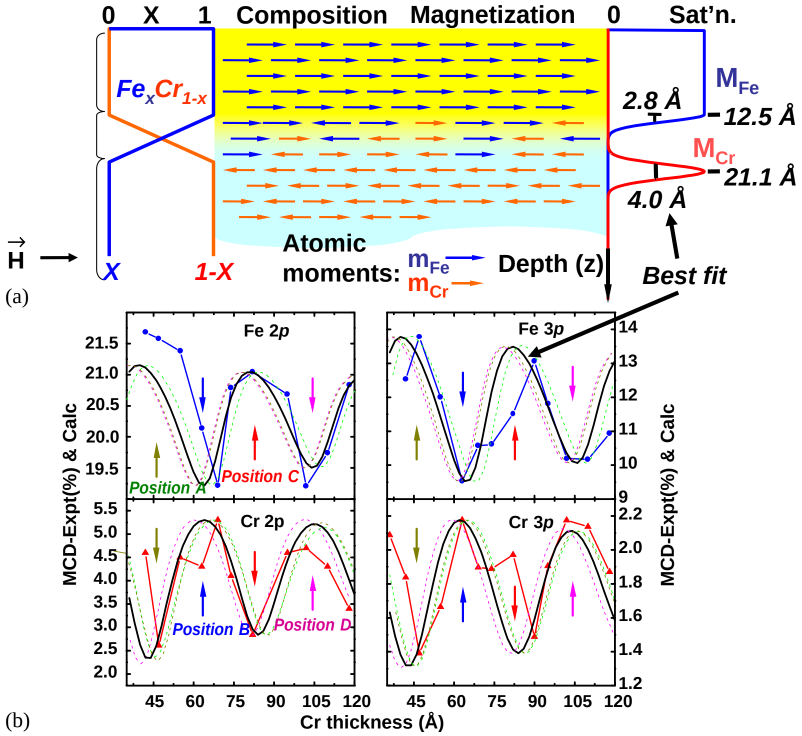

Fig. 6. Soft X-ray experimental results at 825 eV photon energy from the standing wave-wedge method introduced in Fig. 5. By fitting both rocking curve data of Fe/Cr intensity ratios (not shown) and magnetic circular dichroism (MCD) data for Fe and Cr (panel (b)), to depth-resolved X-ray optical calculations [19], the concentration and magnetization profiles through the Fe/Cr interface have been derived [18].

element-specific study of local atomic structure in the bulk of a material, including for example, that around dilute dopant species in more complex materials. But beyond this are other pluses and minuses.

Thompson and Fadley some time ago [22] carried out theoretical simulations in order to compare XPD at 1 and 10 keV, and some of their results are shown in Fig. 8. Here, the simple case of C 1s emission from a vertically oriented CO molecule, which should result in a forward scattering peak (0th order diffraction) and higher-order diffraction features, as shown in Fig. 8(a), is treated. Fig. 8(b) shows that the forward scattering peaks typical of XPD data are clear for both energies, and that the predicted anisotropies in the absence of any vibrational motion of the molecule are about the same for both energies, but the forward peak is significantly narrower at 10 keV. Thus, forward scattering diffraction features are in general expected to be sharper at higher energies. The higher-order diffraction features are, however, weaker at 10 keV. Beyond this, the total scattering cross-section falls off as the energy increases [22], and as a result, the presence of any vibrational broadening tends to quickly reduce the fractional anisotropies in diffraction patterns. Further discussions of the pros and cons of XPD at 10 keV appear in this earlier paper.

Beyond such intramolecular arguments, Fig. 1(b) illustrates another important aspect of HXPD: Bragg-like reflections from crystal planes which produce Kikuchi lines and patterns. The core photoelectron emitter acts like a point source inside the crystal, and for a given set of planes $\{hk\ell\}$ Bragg reflection can occur over two cones, at ± the Bragg angle $\theta_{hk\ell}$ with respect to the planes. Bands of enhanced and deenhanced intensity thus arise for

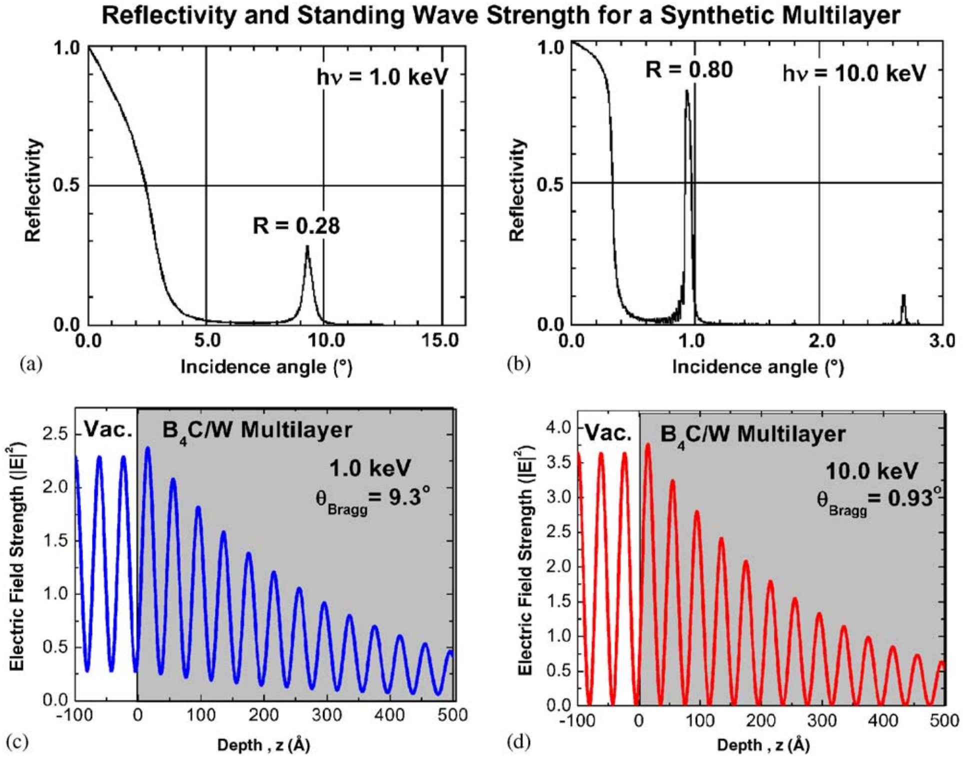

Fig. 7. Theoretical calculations comparing the reflectivity ((a) and (b)) and standing wave modulations ((c) and (d)) above a B$_4$C/W multilayer mirror consisting of 40 bilayers of [B$_4$C-20 Å/W-20 Å] for 1 and 10 keV incident radiation. Calculations in (c) and (d) are due to Yang [19].

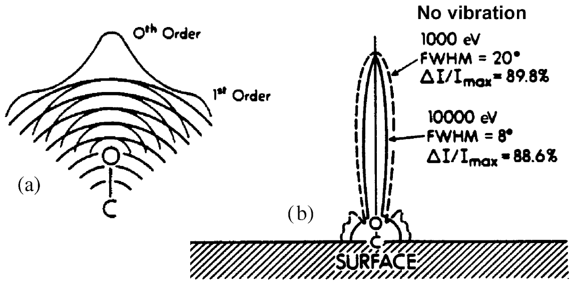

Fig. 8. (a) The fundamental process involved in photoelectron diffraction, illustrated here for C 1s emission in a vertically aligned CO molecule. (b) Comparison of the diffraction profiles expected for emission with electrons of 1000 and 10 000 eV kinetic energy, illustrating the narrowing of the forward scattering (0th order) peak, and the weakening of the higher-order features at the higher energy [22].

each set of low-index planes, with spacings of $\pm\theta_{hk\ell} = \pm\sin^{-1}(\lambda_e/2d_{hk\ell})$, as shown schematically in Fig. 9(a). Such bands are already evident in XPD measurements at about 1 keV, as shown in Figs. 10(a)–(b) based on work by Osterwalder et al. [23] Here, bands of enhanced intensity adjacent to darker side bands are clearly evident in photoemission from both diamond(1 1 1) and Si(1 1 1), with the expected narrowing based on the different lattice constants and thus planar spacings in these two materials. For comparison, we also show data of Pronin et al. [24] from Si(1 1 1) that were obtained with a standard LEED system, with an incident energy of 2 keV. It is clear that the same effects are seen in XPD as in high-energy LEED patterns, in which small inelastic scattering events act to produce the same sort of localized source of outgoing electrons in the LEED experiment as the photoemission process does in XPD. Trehan et al. [25] have also pointed out via model calculations that these Kikuchi-band effects can be described via a typical cluster-based photoelectron diffraction calculation, thus emphasizing that inelastic scattering is not an essential element of such effects in XPD, except in the attenuation of outgoing waves. Some of their results are shown in Fig. 9(b), in which single-scattering cluster XPD calculations for Cu $2p_{3/2}$ emission at 555 eV kinetic energy are compared with the results of simple two-beam Kikuchi-band calculations, with different electron inelastic attenuation lengths. As the attenuation length is increased in theory, the Kikuchi-like features sharpen in both types of calculation, as expected since scattering from a greater number of planes is involved.

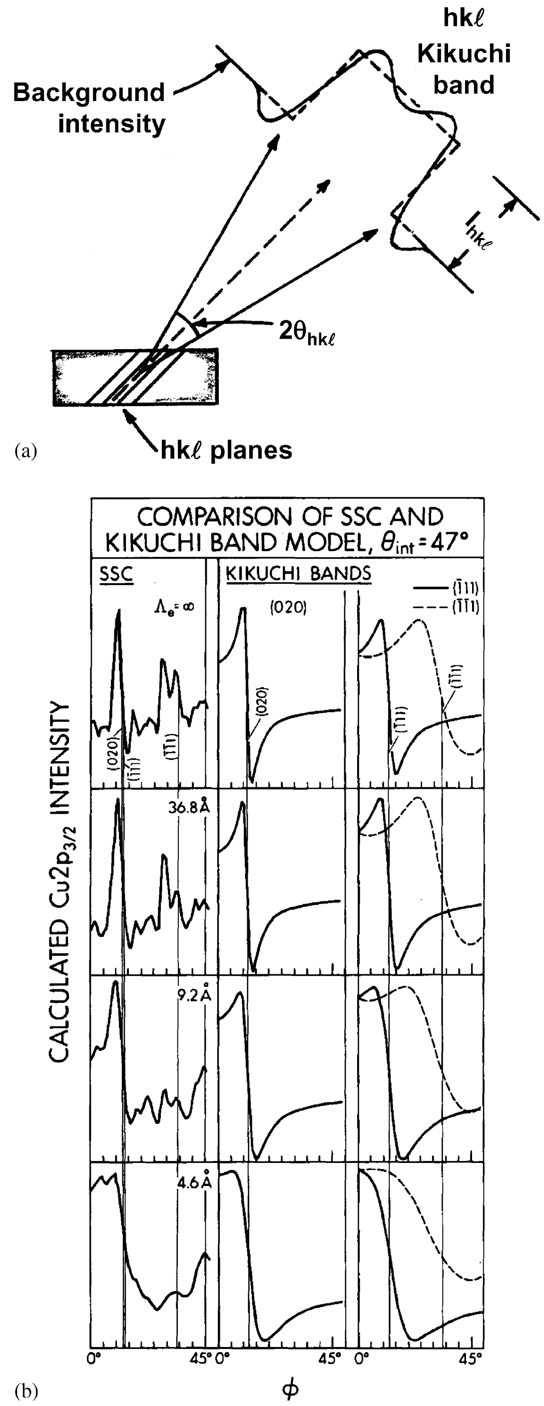

Fig. 9. (a) Qualitative form of the Kikuchi-band profiles expected as photoelectron kinetic energy is increased. (See also Fig. 1(b)). (b) Calculations of azimuthal diffraction profiles based on two models: a single-scattering cluster (SSC) approach to XPD and a simple two-beam Kikuchi-band theory [25]. The case treated is Cu 2p emission with 1487 eV excitation from Cu(0 0 1), at a kinetic energy of 555 eV. The Kikuchi bands are separately calculated for different low-index planes. In both sets of calculations, the inelastic attenuation length Λ_e is systematically varied, so as to illustrate the sharpening of the features for larger values of this parameter, and the equivalence of the two models.

Thus, one expects to see even sharper, more bulk-sensitive Kikuchi-like bands in XPD from bulk samples at 5–15 keV, and these should provide element-specific information on the local atomic environments of each type of atom present. The sensitivity of such features to vibrational motion also should provide a useful element-specific measure of atomic displacements as a function of temperature. However, a final caveat regarding such measurements is in that, in order to obtain sufficient intensity for conveniently short measuring times, the electron optical system may have an acceptance angle that will average over some of the finest structure in these patterns. Compensating this somewhat is the fact that core levels will have much larger cross-sections in the hard X-ray regime than valence levels (see also discussion below), so that reducing the solid angle acceptance of the spectrometer might still be consistent with reasonable intensity.

7. Valence-level studies, photon momentum, phonons, and Brillouin-zone averaging

It is also well known that, on taking the photon energy up to the keV range, one can, for solids

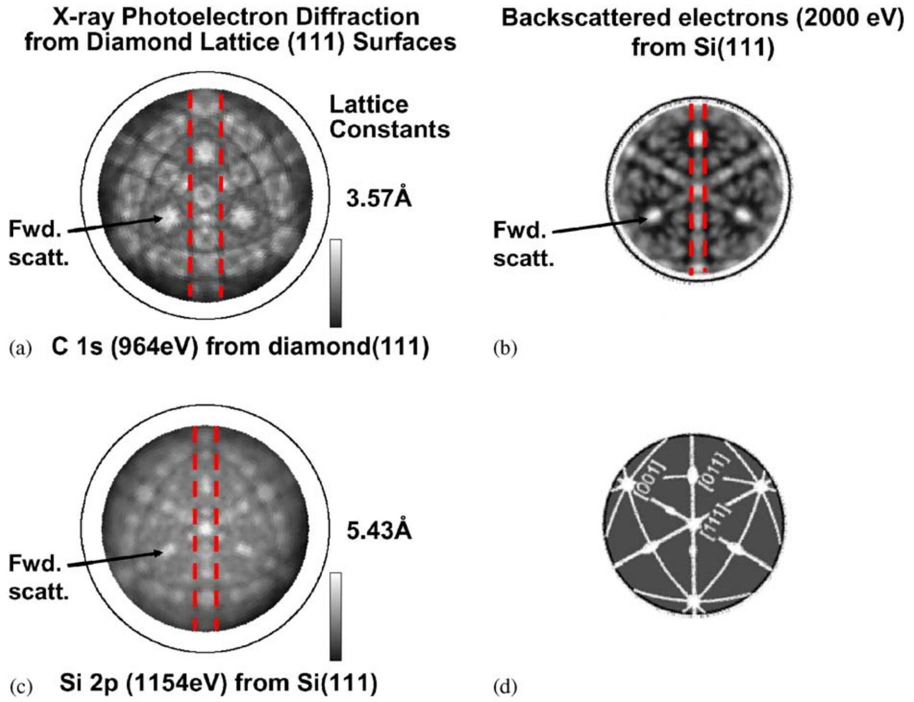

(a) C 1s (964eV) from diamond(111)

(b)

(c) Si 2p (1154eV) from Si(111)

(d)

Fig. 10. Experimental XPD patterns from (a) diamond at 964 eV and (b) Si(1 1 1) at 1154 eV [23] , illustrating the presence of forward scattering features along low-index directions (shown in (d)), as well as Kikuchi-band-like features (highlighted by dashed lines), with narrowing of the latter at higher energy, as expected from Fig. 9(a). Also shown in (c) is a backscattering intensity pattern from Si(1 1 1) at 2 keV [24], with obvious close similarity.

with sufficiently high atomic vibrational amplitudes and/or at sufficiently high temperatures and/or with sufficient angular averaging reach what has been called the "XPS limit" in studying valence levels [26]. This limit implies complete averaging of the spectrum over the valence bands $E(\vec{k})$ of a solid (i.e. Brillouin-zone (BZ) averaging) so as to yield spectra that represent a matrix-element-weighted density of states (DOS). To illustrate the degree to which XPS spectra converge to the density of states, Fig. 11 shows spectra from Ag and Au obtained recently by Siegbahn [27] using monochromatized Al Kα excitation at 1.5 keV, in comparison the theoretical densities of states; the agreement here in fine structure and peak positions, even if not totally in intensity due to residual matrix element effects, is striking.

That many XPS valence spectra at ca. 1 keV excitation are in fact a mixture of the DOS-weighted XPS limit and a "UPS limit" in which wave-vector-conserving direct transitions (DTs) are important and each emission direction corresponds to sampling some region of the BZ was first discussed in detail by Hussain et al. [26], who carried out angle-resolved temperature-dependent measurements on W, a metal of sufficient vibrational rigidity that its XPS spectra at room temperature are estimated to retain roughly 50% wave-vector conserving character. To illustrate the strong influence of vibrational motion on such spectra, Fig. 12 shows spectra obtained from tungsten at two close-lying emission directions that are markedly different at room temperature due to wave-vector conservation and incomplete BZ averaging, but converge to nearly the same DOS-dominated form by 1000 K. We return below to a more quantitative consideration of such phonon-associated effects.

It is also worthwhile to consider the basic one-electron matrix elements involved in the absence of

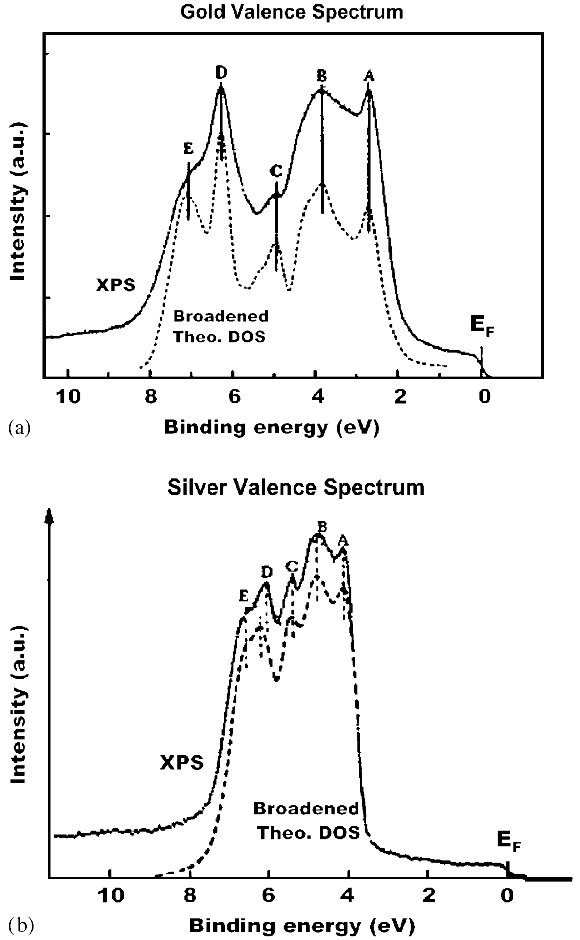

Fig. 11. Valence-band XPS spectra of Ag and Au, obtained with monochromatic X-rays at 1.5 keV by Siegbahn [27], are compared with theoretical densities of states.

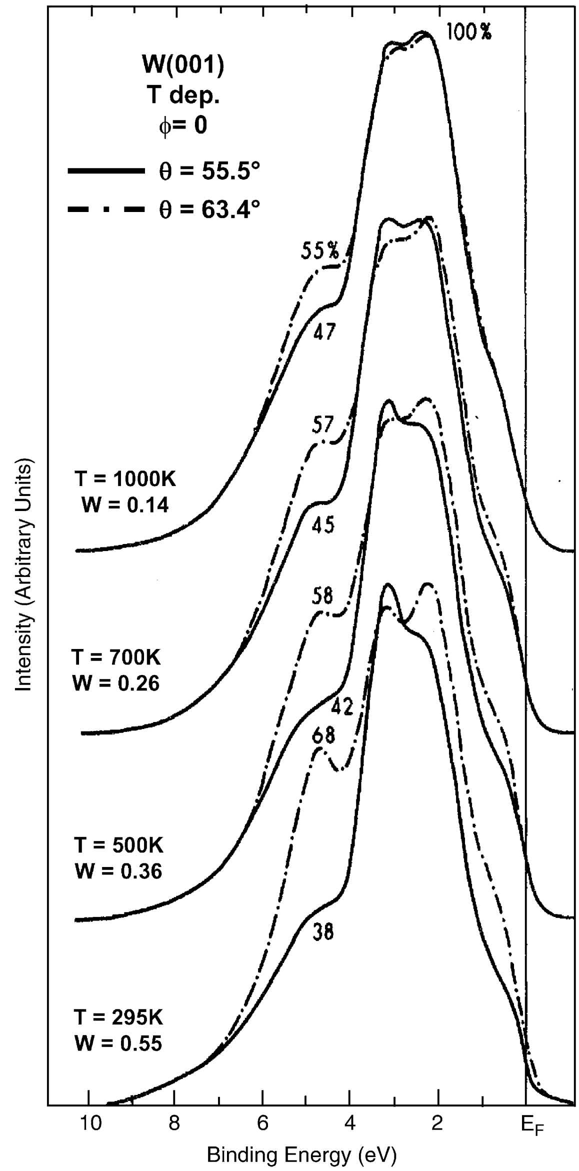

Fig. 12. Experimental illustration of the effect of phonons in producing Brillouin zone averaging in valence-band XPS [26]. With 1.5 keV excitation from W(0 0 1), two close-lying emission directions show distinct differences in their spectra at room temperature due to wave-vector-conserving (direct) transitions, but this difference systematically disappears as temperature is raised to 1000 K, and the density-of-state "XPS limit" is approached. Also shown here are the Debye–Waller factors appropriate to each temperature as a rough estimate of the fraction of transitions which are still direct.

any phonon contributions. From time-dependent perturbation theory and Fermi's Golden Rule, the intensity at a given final energy E^{f} and wave-vector $\vec{k}^{\mathrm{f}}$ resulting from an excitation at E^{i} and $\vec{k}^{\mathrm{i}}$ will be given by

$$I(E^{\mathrm{f}},\vec{k}^{\mathrm{f}}) \propto |\hat{\varepsilon}\cdot\langle E^{\mathrm{f}},\vec{k}^{\mathrm{f}}|\mathrm{e}^{\mathrm{i}\vec{k}_{h\nu}\cdot\vec{r}}\hat{p}|E^{\mathrm{i}},\vec{k}^{\mathrm{i}}\rangle|^2 \tag{6}$$

where $\hat{\varepsilon}$ is the polarization vector of the photon; $k_{h\nu} = 2\pi/\lambda_{h\nu}$ is the wave vector associated with the photon momentum, with direction fixed by the experimental geometry; and $\hat{p}$ is the momentum operator. If $\vec{k}_{h\nu}$ is small with respect to the dimensions of the BZ, which are typically $2\pi/a$ if a is the lattice constant, the dipole approximation is valid, and the exponential inside the matrix element can be assumed constant over the integration. The actual matrix element can then be expressed alternatively in momentum, length, or acceleration forms. However, this approximation is not valid for photon energies of ~500 eV or more, as we now illustrate more quantitatively.

Fig. 13(a) schematically shows a typical transition in tungsten in wave-vector space with a photon energy of 1.25 keV, with the relevant wave-vector selection rule which results from Eq. (6) being

$$\vec{k}^{\mathrm{i}} + \vec{g} + \vec{k}_{h\nu} = \vec{k}^{\mathrm{f}}. \quad (7)$$

Here, $\vec{k}^{\mathrm{i}}$ is the initial electron wave vector inside the BZ; $\vec{g}$ is some reciprocal lattice vector associated with the crystal; and $\vec{k}^{\mathrm{f}} = \vec{p}^{\mathrm{f}}/\hbar$ is the wave vector associated the final photoelectron momentum. For the specific case treated in Fig. 13(a), $\vec{g} = 10(2\pi/a)\hat{y}$, where $\hat{y}$ is a unit vector along the [0 1 0] direction, and $\vec{g}$ will always be that which finally projects $\vec{k}^{\mathrm{f}}$ back into some $\vec{k}^{\mathrm{i}}$ within the BZ.

As a first key point illustrated by this figure, $\vec{k}_{h\nu}$ cannot be neglected in comparison with the size of $\vec{k}^{\mathrm{i}}$ inside the BZ, even at 1.25 keV excitation energy, and it must be allowed for in interpreting spectra. This is really no more than one consequence of being required to go beyond the dipole approximation in describing the photon-electron interaction at such high energies. The experimental effect of the photon wave vector on spectra is illustrated in Fig. 14, in which it has been found necessary to shift one set of spectra obtained in symmetry-equivalent directions above a W(0 0 1) crystal by about 6° in polar angle in order for the two sets to sample the same regions in the BZ, that is to look essentially identical in pairs. The expectation from simple theory is a shift of about 5° that is in excellent agreement with experiment. Such effects will become much more important in HXPS studies of valence bands, provided that any sort of BZ selectivity is still present, and we illustrate this in Fig. 13(b) for the same W emission geometry, but with 10 keV excitation energy. In the XPS limit of complete BZ averaging, the photon momentum will only serve to introduce non-dipole contributions to the basic matrix elements which modulate the DOS, but again, these will need to be considered.

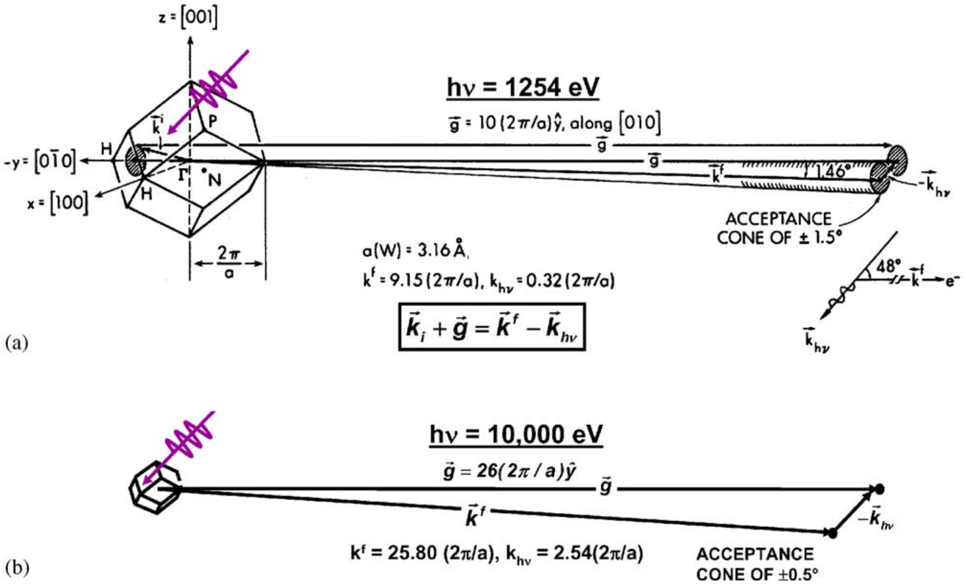

Fig. 13. Illustration of the wave-vector conservation involved in valence-band excitation from W, for (a) 1.25 keV excitation energy and (b) 10.0 keV excitation energy.

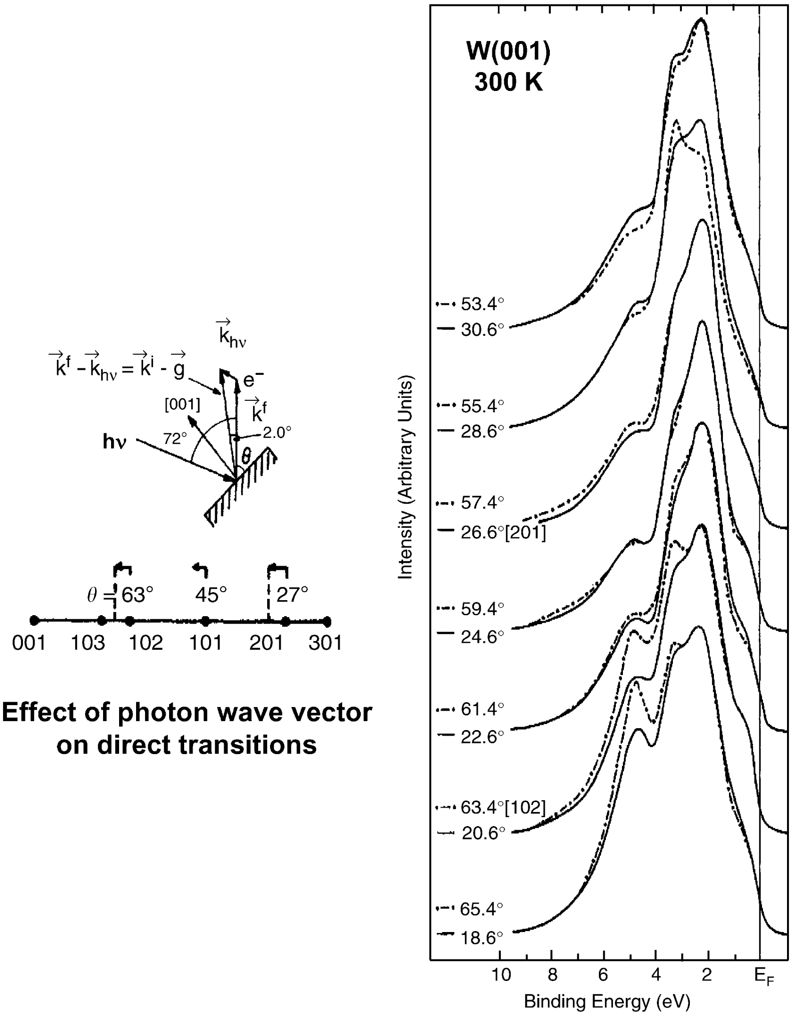

Fig. 14. Experimental verification of the importance of photon wave vector in valence-band XPS, for the case of photoemission from W(0 0 1) with 1.5 keV excitation energy [26]. The photon wave vector correction leads to a shift of about 6° in those symmetry-equivalent emission directions which sample the same region in the Brillouin zone, with the matching shifted pairs of spectra shown at right.

A second effect leading to BZ averaging is the angular acceptance of the analyzer (cf. the shaded discs in Fig. 13), which by itself smears out the set of $\vec{k}^i$ values sampled via direct transitions. Going to higher excitation energy will enhance this effect further, leading to a requirement of smaller solid angle acceptances if any residual direct-transition effects are to be observed.

One must also ask whether the XPS limit will always be reached in valence-band studies at 5–15 keV simply due to phonon effects. Certainly experiment must be the final test, with strong directional and temperature variations of features being qualitative indicators of residual direct transition effects, and cryogenic cooling being of likely benefit in the future in sorting such effects out. But prior studies [26] permit making approximate estimates of this, and suggest that excitation at 5–15 keV will yield rather complete BZ averaging, even before allowance is made for additional averaging effects due to angular resolution. At the most approximate level, the fraction of transitions that remain $\vec{k}$-conserving has been estimated by computing the temperature-dependent Debye–Waller factors $W(T)$ associated with the particular $\vec{g}$ vector involved in the transition

$$W(T) = \exp\left[-\tfrac{1}{3}\langle U^2(T)\rangle\, g^2\right] \tag{8}$$

where $\langle U^2(T)\rangle$ is the three-dimensional mean-squared vibrational displacement, which can be estimated from the Debye model or other more accurate correlated models. The W values obtained from such an analysis are, for example, shown in Fig. 12 for tungsten, which is expected to be among the elements with the highest retention of direct transitions at any temperature [26]. The spectra in Fig. 12 clearly show the convergence of spectral shapes for two close-lying directions as photon effects cause increased BZ averaging. Now applying this type of analysis to excitation of tungsten with 10 keV photons, for which the $\vec{g}$ vector magnitude increases to about $26(2\pi/a)$, yields estimated direct-transition retentions of only 1% at 300 K, 16% at 77 K, and 21% at 4 K. Thus, it is expected that most materials will be very close to the XPS limit when excited with 5–15 keV photons, but perhaps with some residual direct-transition effects still visible via cryogenic cooling.

More accurate models of such phonon effects in angle-resolved photoemission have also been discussed previously [28,29] and Vicente-Alvarez et al. in particular have performed numerical calculations for valence-band photoemission from Al at various photon energies from 105 to 1250 eV which clearly demonstrate the transition from direct-transition-dominated behavior to DOS behavior. Some of their results are shown in Fig. 15, where the polar angular dependence of peak intensities for three different points A, B, and C in $\vec{k}$ but at the same binding energy are plotted for three photon energies. Note the strong direct-transition peaks at 105 eV, where there is also very different behavior of the three points, and the convergence of behavior for 1250 eV. The high-energy behavior of all three $\vec{k}$ points, for which the spectra converge to DOS behavior, is furthermore simply that connected with XPD-like effects that are identical for all states at that energy.

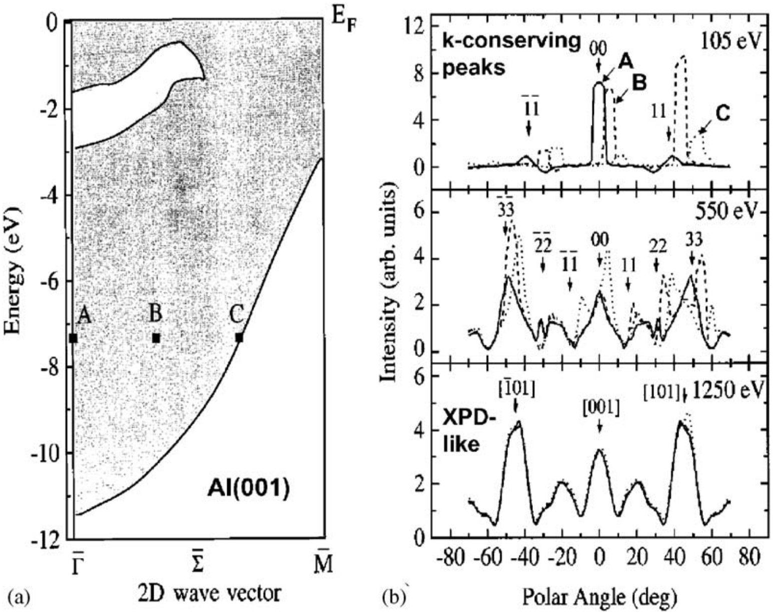

Fig. 15. Theoretical calculations of phonon effects on valence-band photoemission from Al, illustrating the gradual transition from direct-transition behavior to density-of-states behavior [29]. (a) The projected bulk bands of Al, with three $\vec{k}$ points *A*, *B*, and *C* at the same energy E^i for which calculations were carried out. (b) Azimuthal scans of intensity for emission from those $\vec{k}$ points, at photon energies of 105, 550, and 1250 eV.

These results can be compared to a parallel, and prior, experimental studies that led to what can be termed valence photoelectron diffraction (VPD)[30,31]. To illustrate the connection of this theoretical analysis with the experiment, Fig. 16 shows core and valence XPS spectra from aluminum obtained by Osterwalder et al. [30], together with an azimuthal scan of the energy-integrated VB intensity and the Al 2s core intensity. Both VB and core intensities exhibit essentially the same angular distribution, which is describable in terms of XPD. Similar results have also been found by Herman et al. [31] for Ge valence and core spectra in XPS.

No calculations of vibrational effects on XPS valence spectra at the level of accuracy of those of Vicente-Alvarez et al. have been carried out for other elements or for energies as high as 5–15 keV, but further analyses of this type would certainly be very desirable. One expectation would nonetheless be that, once the XPS limit is reached, the integrated valence-band intensities, or even intensities at a fixed binding energy in a spectrum (cf. Fig. 15) would exhibit HXPD effects such as those discussed in Section 6: forward scattering peaks along low-index directions and Kikuchi bands.

Finally, we consider the nature of the matrix elements in Eq. 6, in terms of the region in space that is primarily involved, as discussed also by Solterbeck et al. [32] In general, because of the high energy of the photoelectron, its oscillations in space, with wavelength $\lambda^f = 2\pi/k^f$, which is only about 0.10–0.15 Å for 5000–10,000 eV energies, are very short in scale relative to those of outer valence electronic states. Thus, there tends to be a net cancellation in matrix element contributions from the positive and negative portions of the photoelectron wave that are multiplied by the much more slowly varying valence wave function. This is the reason core levels, which oscillate much more rapidly in radius, maintain larger cross-sections as photon energy increases. A further implication of this kind of argument for valence band studies is that HXPS spectra should be much more sensitive to those portions of valence electron wave functions that are nearest the nucleus, as discussed by Woicik in another article in this volume [17].

In summary, from prior XPS work on valence levels, it seems likely that HXPS in the 5–15 keV

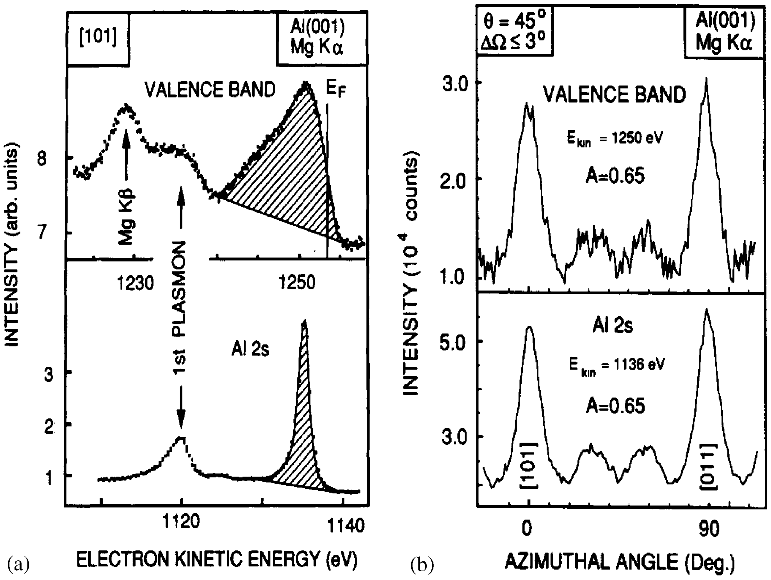

Fig. 16. Azimuthal-scan experimental data for valence-band and core photoemission from Al [30]: Valence-band (a) and core Al 2s (b) spectra, and the azimuthal dependence of the energy-integrated valence-band intensity (c) and the core intensity (d).

range will for many, if not most, cases yield spectra in the XPS limit of zone-averaged densities-of-states with matrix element modulation. Variable-temperature studies going to the lowest possible temperatures, as well as more accurate theoretical modeling, would certainly be of interest in sorting out the phonon contributions to zone averaging. Beyond this, analyzer angular acceptance, also leading to zone averaging, represents another major factor which would be difficult to avoid without reducing intensities too much for practical spectroscopy. Finally, non-dipole effects need to be considered, both via the contribution of the photon wave vector to the conservation equation and other more subtle factors in the matrix elements themselves. Even if all such data is found to be in the XPS limit however, such density-of-states information should be extremely useful, especially in view of the greater bulk sensitivity at these higher energies. Beyond this, single crystal or multilayer standing wave effects such as those discussed in Section 5 should be most interesting in deriving element-specific contributions to the valence electronic structure [17], as well as the variation with depth of densities of states, e.g. through multilayer structures.

8. Concluding remarks

By suitable instrumentation improvements in SR sources, electron optical systems, and detectors, HXPS in the 5–15 keV regime has now become a feasible experiment, including both core and valence-level measurements.

Going to such high excitation energies permits measurements that are much more bulk in nature, with mean excitation depths in the 50–100 Å range. The necessity for careful surface preparation is thus much reduced, but not completely eliminated for more sensitive materials.

Varying the degree of surface sensitivity by changing the electron takeoff angle should be more easily quantifiable than at lower energies, due to more forward peaked elastic electron scattering and the reduced influence of the inner potential at the surface.

Using grazing X-ray incidence, at or somewhat above the onset of total reflection should be of use in reducing the inelastic backgrounds underneath spectra.

X-ray standing waves, created by Bragg reflection from either crystal planes or synthetic multilayer mirrors, constitute a very powerful position-resolved probe of element-specific densities of states [17], or composition and magnetization near buried interfaces.

Core-level angular distributions above single-crystal samples will exhibit photoelectron diffraction effects, including both a sharpening of forward scattering features and the presence of Kikuchi-band fine structure due to Bragg reflection of photoelectrons from crystal planes. These effects should provide element-specific local structure information, provided that the solid angle of acceptance of the spectrometer can be reduced sufficiently to see them clearly.

Valence-level studies at such high excitation energies will tend toward the "XPS limit" for which initial states over the entire BZ are sampled, and spectra are matrix-element-modulated densities of states. This is due to a combination of phonon effects and the angular acceptance of the spectrometer. The photon momentum and other non-dipole effects in matrix elements will need to be considered in analyzing such data. Nonetheless, much useful information on bulk densities of states should be derivable.

References

[1] K. Siegbahn, et al., ESCA-Atomic, Molecular, and Solid-State Structure Studied by Means of Electron Spectroscopy, Almqvist and Wiksells AB, Stockholm, 1967 (and earlier papers cited therein).

[2] P. Pianetta, I. Lindau, Nature 250 (1974) 214.

[3] C. Dallera, L. Duo, L. Braicovich, G. Panaccione, G. Paolicelli, B. Cowie, J. Zegenhagen, Appl. Phys. Lett. 85 (2004) 4532;
P. Torelli, et al., Rev. Sci. Inst. 76 (2005) 023909 (and other articles in this issue).

[4] S.B.M. Hagstrom, C.S. Fadley, in: L. Azaroff (Ed.), X-ray Spectroscopy, McGraw-Hill Publishing Co., New York, 1974 (Chapter 8, including a detailed discussion of the interplay of retardation, resolution, and intensity);
C.S. Fadley, in: C.R. Brundle, A.D. Baker (Eds.), Electron

Spectroscopy: Theory, Techniques, and Applications, vol. II, Academic Press, London, 1978 (Chapter 1).

[5] (a) A. Jablonski, C.J. Powell, J. Vac. Sci. Tech. A 21 (2003) 274 and earlier references therein; (b) C.J. Powell, Private communication.

[6] (a) S.T. Manson, Private Communication; (b) J.H. Scofield, Lawrence Livermore Laboratory Report UCRL-51326 (1973), also available for download at http://electron.lbl.gov/software/software.html

[7] M.B. Trzhaskovskaya, V.I. Nefedov, V.G. Yarzhemsky, Atom. Data Nucl. Data Tables 82 (2002) 257.

[8] J.-M. Bussat, C.S. Fadley, Z. Hussain, A.W. Kay, G. Lebedev, B.A. Ludewigt, G. Meddeler, A. Nambu, M. Press, H. Spieler, B. Turko, M. West, G. Zizka, AIP Conf. Proc. 705 (2004) 945.

[9] S. Tanuma, C.J. Powell, D.R. Penn, Surf. Interf. Anal. 21 (1994) 165;
S. Tanuma, C.J. Powell, D.R. Penn, Surf. Interf. Anal. 35 (2003) 268 (results of the TPP-2M model extrapolated to higher energies as $E_{\mathrm{kin}}^{0.75}$).

[10] W.S.M. Werner, L. Kover, J. Toth, D. Varga, J. Electron. Spectrosc. 122 (2002) 103
C.J. Powell, W.S.M. Werner, Private communication.

[11] C.S. Fadley, in: S. Davison (Ed.), Progress in Surface Science, vol. 16, Pergamon Press, New York, 1984 p. 275.

[12] B.L. Henke, Phys. Rev. A 6 (1972) 94.

[13] J. Kawai, M. Takami, M. Fujinami, Y. Hashiguchi, S. Hayakawa, Y. Gohshi, Spectrochim. Acta B 47 (1992) 983;
M.J. Chester, T. Jach, Phys. Rev. B 48 (1993) 17262;
T. Jach, E. Landree, Surf. Interf. Anal. 31 (2001) 768.

[14] Y. Iijima, K. Miyoshi, S. Saito, Surf. Interf. Anal. 27 (1999) 35È42.

[15] Center for X-Ray Optics, Lawrence Berkeley National Laboratory, website http://www.cxro.lbl.gov/optical_constants/

[16] C.-Y. Kim, M.J. Bedzyk, E.J. Nelson, J.C. Woicik, L.E. Berman, Phys. Rev. B 66 (2002) 85115;
J.C. Woicik, E.J. Nelson, L. Kronik, M. Jain, J.R. Chelikowsky, D. Heskett, L.E. Berman, G.S. Herman, Phys. Rev. Lett. 89 (2002) 077401.

[17] J. Woicik, Nucl. Instr. and Meth. A, this volume.

[18] S.-H. Yang, B.S. Mun, A.W. Kay, S.-K. Kim, J.B. Kortright, J.H. Underwood, Z. Hussain, C.S. Fadley, Surf. Sci. Lett. 461 (2000) L557;
S.-H. Yang, B.S. Mun, N. Mannella, S.-K. Kim, J.B. Kortright, J. Underwood, F. Salmassi, E. Arenholz, A. Young, Z. Hussain, M.A. Van Hove, C.S. Fadley, J. Phys. Condens. Matter 14 (2002) L406.

[19] S.-H. Yang, Computer program for simulating standing-wave excited spectroscopy, to be published.

[20] C.S. Fadley, in: R.Z. Bachrach (Ed.), Chapter in Synchrotron Radiation Research: Advances in Surface and Interface Science, Plenum Press, New York, 1992.

[21] Two X-ray photoelectron diffraction programs are available for online usage or as freeware at: http://electron.lbl.gov/~edac/ or http://electron.lbl.gov/mscdpack/mscdpack.html. These are limited to about 2 keV in maximum energy, however.

[22] K.A. Thompson, C.S. Fadley, J. Electron. Spectrosc. 33 (1984) 29.

[23] J. Osterwalder, R. Fasel, A. Stuck, P. Aebi, L. Schlapbach, J. Electron. Spectrosc. 68 (1994) 1.

[24] I.I. Pronin, D.A. Valdaitsev, N.S. Faradzhev, M.A. Gomoyunova, P. Luches, S. Valeri, Appl. Surf. Sci. 175 (2001) 83.

[25] R. Trehan, J. Osterwalder, C.S. Fadley, J. Electron. Spectrosc. 42 (1987) 187.

[26] Z. Hussain, S. Kono, C.S. Fadley, Phys. Rev. 22 (1980) 3750.

[27] K. Siegbahn, J. Electron. Spectrosc. 137–140 (2004) 3.

[28] R.C. White, C.S. Fadley, M. Sagurton, P. Roubin, D. Chandesris, J. Lecante, C. Guillot, Z. Hussain, Phys. Rev. B 35 (1987) 1147.

[29] M.A. Vicente Alvarez, H. Ascolani, G. Zampieri, Phys. Rev. B 54 (1996) 14703.

[30] J. Osterwalder, T. Greber, S. Hüfner, L. Schlapbach, Phys. Rev. Lett. 64 (1990) 2683.

[31] G.S. Herman, T.T. Tran, K. Higashiyama, C.S. Fadley, Phys. Rev. Lett. 68 (1992) 1204.

[32] C. Solterbeck, W. Schattke, J.-W. Zahlmann-Nowitzki, K.-U. Gawlik, L. Kipp, M. Skibowski, C.S. Fadley, M.A. Van Hove, Phys. Rev. Lett. 79 (1997) 4681.